Research Square

Preprints are preliminary reports that have not undergone peer review.
They should not be considered conclusive, used to inform clinical practice,
or referenced by the media as validated information.

DCE-MRI-derived peritumoral and habitat radiomics for preoperative prediction of p53-abnormal endometrial cancer: a dual-center retrospective study with external validation

Huijie Dai
Qilu Hospital of Shandong University
Wenxiu Guo
Tianjin Medical University Cancer Institute and Hospital
Yao Liu
Shandong Provincial Hospital Affiliated to Shandong First Medical University
Baoxing Yan
Xintai Hospital of Traditional Chinese Medicine
Binglin Lyu
Qilu Hospital of Shandong University
Fang Wang
Qilu Hospital of Shandong University
Jie Jiang
qljiangjie@sdu.edu.cn

Qilu Hospital of Shandong University

Research Article

Keywords: endometrial cancer, p53-abnormal, magnetic resonance imaging, habitat radiomics, peritumoral radiomics, molecular classification

Posted Date: August 26th, 2026

DOI: https://doi.org/10.21203/rs.3.rs-10730684/v1

License: This work is licensed under a Creative Commons Attribution 4.0 International License. Read Full License

Additional Declarations: No competing interests reported.

Abstract

Background

Preoperative identification of p53-abnormal (p53abn) endometrial cancer is important for molecular risk stratification, yet biopsy-based testing and p53 immunohistochemistry may be limited by sampling and interpretive variability. This study aimed to develop and externally validate a dynamic contrast-enhanced MRI (DCE-MRI) fusion model integrating peritumoral radiomics, intratumoral habitat features, and clinical predictors for noninvasive prediction of p53abn endometrial cancer.

Methods

This retrospective dual-center study included 498 patients with surgically confirmed endometrial cancer and sequencing-based molecular classification. Patients from Institution 1 were assigned to a training cohort (n = 351) and an internal validation cohort (n = 86), and patients from Institution 2 formed an external validation cohort (n = 61). Radiomic features were extracted from the whole tumor, 3-mm and 5-mm peritumoral regions, and three unsupervised intratumoral habitat subregions. After reproducibility assessment, statistical filtering, correlation analysis, and least absolute shrinkage and selection operator selection, single-domain models were developed. A fusion model combined clinical predictors with the 5-mm peritumoral and habitat radiomics scores. Performance was assessed using discrimination, calibration, decision curve analysis, reclassification metrics, and shapley additive explanations (SHAP) interpretation.

Results

The habitat model showed the most stable single-domain performance, with AUCs of 0.831, 0.813, and 0.788 in the training, internal validation, and external validation cohorts, respectively. The fusion model achieved AUCs of 0.891, 0.885, and 0.863, with sensitivities of 0.882, 0.765, and 0.889 and negative predictive values of 0.974, 0.925, and 0.968, respectively. Brier scores were 0.078, 0.095, and 0.110. SHAP analysis identified the habitat and 5-mm peritumoral radiomics scores as the dominant contributors to prediction.

Conclusions

A DCE-MRI fusion model integrating clinical, peritumoral, and habitat radiomics demonstrated good discrimination and external generalizability for preoperative p53abn prediction. The model may serve as a noninvasive adjunct to molecular testing for preoperative risk stratification.

Background

Endometrial cancer (EC) is one of the most common gynecologic malignancies in women, and its disease burden continues to increase [1]. The proportion of cases diagnosed in young women is also rising, with 4% of patients being younger than 40 years [2]. Although surgery-based multidisciplinary treatment has substantially improved the clinical management of patients with early-stage disease [3], the prognosis of advanced and recurrent EC remains unsatisfactory [4].

The traditional Bokhman dualistic model cannot fully explain the molecular heterogeneity of EC. By contrast, The Cancer Genome Atlas (TCGA) classification, based on deep sequencing, has reshaped risk stratification by defining four molecular subtypes, including the highly aggressive p53-abnormal (p53abn) subtype with poor prognosis [5–10]. However, its high testing cost and technical complexity have substantially limited its widespread implementation in real-world clinical practice. From the perspective of objective criteria for clinical intervention, p53abn subtype not only indicates poor prognosis but also represents an absolute contraindication to progestin-based fertility-sparing treatment in young patients [11]. Because this phenotype is often associated with intrinsic progestin resistance and a very high risk of disease progression, accurate exclusion of p53abn before treatment is a core prerequisite for determining eligibility for conservative management [12].

Accordingly, classification systems such as ProMisE have enabled clinical translation of molecular classification through mismatch repair (MMR)/p53 immunohistochemistry (IHC) combined with targeted POLE sequencing. However, as a surrogate for TP53 genetic

alterations, p53 IHC is susceptible to misclassification caused by subjective interpretation related to staining procedures and abnormal expression patterns, such as subclonal expression and cytoplasmic expression [13–15]. More importantly, because of pronounced spatial heterogeneity, conventional invasive local biopsy is highly prone to sampling error, leading to discordance between preoperative assessment and final pathology in nearly 20% of cases [16–18]. Given the multiple limitations of current molecular testing in terms of cost, subjective interpretation, and sampling representativeness [19–20], the development of a noninvasive predictive model is particularly necessary.

Magnetic resonance imaging (MRI) is the preferred modality recommended by the International Federation of Gynecology and Obstetrics (FIGO) for preoperative assessment of EC. However, qualitative MRI assessment is susceptible to interobserver variability and lacks objective quantitative indicators [21–22]. Conventional radiomics can extract high-throughput quantitative features from medical images. Nevertheless, previous studies predicting p53abn molecular subtype using averaged whole-tumor representations, such as conventional MRI sequences or whole-tumor apparent diffusion coefficient (ADC) histogram analysis, have shown relatively limited discriminatory performance [23–31]. This limitation is mainly attributable to the fact that conventional radiomics usually treats the tumor as a homogeneous entity, thereby overlooking the spatial variation of intratumoral phenotypes.

Because of rapid proliferation and aberrant angiogenesis, the highly aggressive p53abn subtype often exhibits substantial structural and microenvironmental heterogeneity within the tumor, such as the coexistence of necrotic areas and regions of high cellular density [32]. In contrast, habitat radiomics can quantify distinct functional subregions through unsupervised clustering, thereby more precisely capturing spatial heterogeneity that may be obscured by whole-tumor analysis [33–35]. Meanwhile, remodeling of the peritumoral microenvironment beyond the tumor boundary also profoundly reflects tumor invasion, progression, and host–tumor interactions [36].

Given the strong complementarity between intratumoral habitat analysis and peritumoral microenvironmental information in characterizing the spatial tumor phenotype, this study aimed to integrate clinical characteristics, conventional radiomics from intratumoral and different peritumoral regions, and habitat radiomics to develop and validate a multidimensional preoperative fusion model. This model was designed to overcome the blind spots of biopsy sampling, substantially improve the accuracy of preoperative p53abn subtype prediction, and support the implementation of precision perioperative diagnostic and therapeutic strategies.

Methods

Study design and participants

This retrospective dual-center study included 615 patients with EC treated at Qilu Hospital of Shandong University (Institution 1) between January 2018 and December 2024, and 90 patients with EC treated at Tianjin Medical University Cancer Institute and Hospital (Institution 2) between January 2024 and December 2025. The inclusion criteria were as follows: (1) pathologically confirmed EC after surgery, with standard staging surgery performed; (2) completion of sequencing-based molecular classification, including assessment of POLE mutation status, TP53 mutation status, and microsatellite instability (MSI) status; and (3) availability of high-quality preoperative MRI data, including clear images and complete dynamic contrast-enhanced MRI (DCE-MRI) sequences. The exclusion criteria were as follows: (1) incomplete clinicopathological data; (2) poor image quality due to severe artifacts or inability to perform accurate segmentation; (3) receipt of non-surgical treatment before MRI examination, such as neoadjuvant chemotherapy or high-dose progestin therapy; and (4) coexistence of malignancies from other organ systems. After screening according to the inclusion and exclusion criteria, 498 patients were finally included. Among them, 437 patients from Institution 1 were assigned to the internal dataset and randomly divided at an 8:2 ratio into a training cohort (n = 351) and an internal validation cohort (n = 86), while 61 patients from Institution 2 were assigned to the external validation cohort.

This study was conducted in accordance with the Declaration of Helsinki and was approved by the Scientific Research Ethics Committee of Qilu Hospital of Shandong University (approval number: KYLL-202210-05501). The requirement for written informed consent was waived by the approving ethics committee because of the retrospective nature of the study. All clinical and imaging data were de-identified. The detailed patient recruitment and screening workflow is shown in Fig. 1.

MRI acquisition and interpretation

All patients underwent preoperative pelvic MRI on a 3.0-T system (MAGNETOM Verio, Siemens, Germany) using an 8-channel pelvic phased-array surface coil. All patients fasted for at least 4 hours before the examination. The MRI sequence included in the present analysis was sagittal DCE-MRI.

Image preprocessing and segmentation

All MRI images were exported in Digital Imaging and Communications in Medicine (DICOM) format from the picture archiving and communication system (PACS). N4 bias field correction was first performed to reduce signal intensity inhomogeneity. The images were then resampled to an isotropic voxel size of 1 mm × 1 mm × 1 mm using nearest-neighbor interpolation to reduce intercenter differences in spatial resolution, followed by Z-score normalization for gray-level standardization.

On DCE-MRI, MRI-visible tumors were defined as abnormally enhancing lesions originating from the endometrium and located within the endometrial cavity or at the endometrial–myometrial junction. These lesions typically showed slower and lower enhancement than the adjacent myometrium and were most clearly visualized on post-contrast images acquired approximately 90 seconds after enhancement, when tumor–myometrium contrast was optimal. In cases with myometrial invasion, early dynamic contrast-enhanced images showed interruption or irregularity of the normal subendometrial enhancement band.

Two experienced radiologists, blinded to the pathological results, manually delineated the tumor volume of interest (VOI) slice by slice on DCE-MRI using ITK-SNAP software. To evaluate radiomic features of the peritumoral microenvironment, the original tumor VOI was isotropically expanded outward by 3 mm and 5 mm, respectively. The original tumor VOI was then subtracted from each expanded VOI to generate the Peri3mm and Peri5mm peritumoral ring regions.

Radiomic feature extraction and habitat partitioning

For habitat analysis, a three-dimensional 6-neighborhood local feature extraction strategy was used. Specifically, for each voxel within the VOI, the six directly adjacent voxels in the anterior, posterior, left, right, superior, and inferior directions were selected together with the central voxel to form a local neighborhood. A 19-dimensional feature vector was then extracted from this neighborhood to characterize the local imaging properties of each voxel **(Additional file : Supplementary Figure S1)**.

At the cohort level, K-means clustering was applied. Because previous habitat radiomics studies have commonly used three habitat subregions to balance heterogeneity characterization and interpretability, the number of clusters in this study was set from 2 to 4. The optimal cluster number was determined using the Calinski–Harabasz (CH) index, thereby ensuring the robustness of the clustering results and partitioning the whole tumor into physiologically heterogeneous subregions, defined as habitats.

Image feature extraction was performed in strict accordance with the guidelines of the Imaging Biomarker Standardization Initiative (IBSI), using the PyRadiomics package in Python (version 3.0.1). Features were extracted separately from the whole tumor (Tumor), the 3-mm peritumoral region (P3), the 5-mm peritumoral region (P5), and each habitat subregion. To assess segmentation reproducibility, 50 patients were randomly selected from the training cohort and independently re-segmented by two radiologists 1 month after the initial delineation. Intra- and interobserver intraclass correlation coefficients (ICCs) were calculated, and only features with ICCs > 0.90 were retained for subsequent analysis.

Feature selection and model development

All feature preprocessing and dimensionality reduction procedures were performed exclusively in the training cohort. For the four feature modules, including Tumor, P3, P5, and Habitat, Z-score standardization was first applied. Features with statistically significant differences were identified using the t test or Mann–Whitney U test, as appropriate ($P < 0.05$). Spearman correlation analysis was then performed to remove highly correlated features ($|r| > 0.90$). The remaining features were further reduced using the least absolute shrinkage and selection operator (LASSO) method. Ten-fold cross-validation was performed to determine the optimal regularization parameter (λ), and features with nonzero coefficients at the optimal λ were selected.

For each imaging feature domain, four machine-learning classifiers were evaluated, including adaptive boosting (AdaBoost), logistic regression (LR), multilayer perceptron (MLP), and support vector machine (SVM). Based on the performance in the internal validation

cohort, a representative model was selected for each of the Tumor, P3, P5, and Habitat feature domains. The radiomics score for each feature domain was defined as the model-derived predicted probability of p53abn.

Clinical predictors were selected in the training cohort using univariable and multivariable logistic regression analyses. Variables retained after multivariable analysis were used to construct the clinical model. To assess the incremental value of different spatial imaging information, logistic regression was further used to integrate clinical features, the Peri5mm Rad-score, and the Habitat Rad-score to construct the fusion model. The final models evaluated in this study included the Clinical model, Tumor model, P3 model, P5 model, Habitat model, and Fusion model.

Statistical analysis

Statistical analyses were performed using R version 4.5.2 and Python 3.10.4. Continuous variables are presented as medians with interquartile ranges, and categorical variables are presented as frequencies and percentages. Between-group comparisons of categorical variables were performed using the Pearson χ^2 test or Fisher's exact test, whereas continuous variables were compared using the Kruskal–Wallis test.

Model discrimination was evaluated using the area under the receiver operating characteristic curve (AUC) and its 95% confidence interval (CI). Classification performance was assessed using accuracy, sensitivity, specificity, positive predictive value, negative predictive value, F1-score, Youden index, and Cohen's kappa. AUCs between different models were compared using the DeLong test. Model calibration was evaluated using calibration curves, the Hosmer–Lemeshow test, calibration intercept, calibration slope, and Brier score. Decision curve analysis (DCA) was used to assess the clinical utility of the models. The net reclassification improvement (NRI) and integrated discrimination improvement (IDI) were used to quantify the incremental predictive value of the fusion model over the reference models. Model interpretability was assessed using a nomogram and SHAP analysis. All statistical tests were two-sided, and $P < 0.05$ was considered statistically significant.

Use of artificial intelligence tools

Artificial intelligence tools were used only for language polishing and preliminary figure layout assistance. The authors reviewed, edited, and approved all AI-assisted content and take full responsibility for the final manuscript.

Results

Patient characteristics

A total of 498 patients with EC were included in this study, with a median age of 55 years (IQR, 51–61 years). The proportions of patients with p53abn in the training, internal validation, and external validation cohorts were 14.53% (51/351), 19.77% (17/86), and 14.75% (9/61), respectively, with no statistically significant difference among the three cohorts. To assess the concordance of p53 IHC with sequencing-based TP53 status, we compared paired results in the dual-center cohort. The overall discordance rate was 10% **(Additional file : Supplementary Figure S2)**. This finding illustrates the potential for misclassification when p53 IHC is used as a surrogate marker and supports the use of molecular sequencing as the reference standard in this study.

Regarding baseline clinical characteristics, most variables were relatively balanced across the three cohorts, including age, body mass index (BMI), menopausal status, hypertension, diabetes, family history of cancer, and most tumor markers (all $P > 0.05$). However, neuron-specific enolase (NSE; $P < 0.001$), albumin ($P < 0.001$), and hemoglobin (Hb; $P = 0.002$) levels differed significantly among the three cohorts **(Additional file : Supplementary Table S1)**. Given the real-world observational design of this study, these baseline fluctuations across centers and time periods objectively reflect heterogeneous clinical practice settings. Therefore, we did not artificially modify or exclude these differing covariates, thereby maximizing the evaluation of model generalization and validation ability in complex real-world populations. Univariable and multivariable logistic regression analyses showed that hypertension and Hb were independent clinical predictors of p53abn, with the corresponding odds ratios (ORs) and 95% confidence intervals (CIs) shown in **Additional file : Supplementary Table S2.**

Habitat partitioning and feature selection

To evaluate the validity of tumor partitioning, we tested cluster numbers ranging from 2 to 4. Among the predefined candidate cluster numbers (K = 2–4), K = 3 achieved the highest CH index (987,266.294) and the lowest Davies–Bouldin index (1.172), indicating an optimal balance between intercluster separation and intracluster compactness. Although K = 2 yielded the highest silhouette coefficient (0.388), it divided the tumor into only two habitat subregions, which may be insufficient to adequately characterize the intratumoral spatial heterogeneity associated with p53abn. Therefore, considering the clustering evaluation metrics, habitat interpretability, and the principle of avoiding excessive fragmentation, the optimal number of tumor subregions in this study was determined to be three **(Additional file : Supplementary Table S7)**.

Subsequently, radiomic features were extracted from four spatial feature domains on DCE-MRI, including the Tumor, P3, P5, and the habitat subregions. A total of 1,834 radiomic features were extracted from each of the Tumor, P3, and P5 regions. For the Habitat feature domain, 1,834 features were extracted from each habitat subregion, yielding 5,502 habitat features across the three habitat subregions. Overall, 11,004 candidate radiomic features were initially generated across the four spatial feature domains. After reproducibility assessment, statistical screening, correlation-based redundancy removal, and LASSO regression with 10-fold cross-validation, the final feature subsets were used to construct region-specific models.

Single-domain model development and validation

Regarding algorithm selection, AdaBoost showed the best performance for the Tumor model, with an AUC of 0.687 (95% CI, 0.544–0.830) in the internal validation cohort. For the P3 model, AdaBoost demonstrated the strongest generalization ability, with AUCs of 0.765 (95% CI, 0.698–0.833) in the training cohort and 0.682 (95% CI, 0.530–0.833) in the internal validation cohort. For the P5 model, the MLP algorithm showed favorable discriminatory performance yielding an AUC of 0.786 (95% CI, 0.680–0.892), an accuracy of 0.686, a sensitivity of 0.882, and a specificity of 0.638 in the internal validation cohort. For the Habitat model, the LR algorithm showed robust performance, with an AUC of 0.813 (95% CI, 0.717–0.909), an accuracy of 0.733, a sensitivity of 0.647, and a specificity of 0.754 in the internal validation cohort.

Accordingly, AdaBoost was selected as the final classifier for the Tumor and P3 models, MLP was selected for the P5 model, and the more robust LR algorithm was selected for the Habitat model.

In the evaluation of single-domain radiomics models, the Habitat model showed the most stable performance across the three cohorts, with AUCs of 0.831 (95% CI, 0.776–0.885), 0.813 (95% CI, 0.717–0.909), and 0.788 (95% CI, 0.597–0.980) in the training, internal validation, and external validation cohorts, respectively. Although DeLong tests showed no statistically significant differences in AUC between the P5 and P3 models in any cohort (all $P > 0.05$), the P5 model demonstrated greater stability and predictive performance in the training and internal validation cohorts. Therefore, the P5 model was ultimately selected as the representative peritumoral model for subsequent fusion modeling **(Additional file : Supplementary Table S3)**.

Fusion model performance and incremental value

To further improve predictive performance, this study integrated clinical features, the 5-mm peritumoral radiomics score (Peri5mm Rad-score), and the habitat radiomics score (Habitat Rad-score) to construct a multidimensional fusion model. The fusion model achieved the highest AUC values across all three cohorts, with AUCs of 0.891 (95% CI, 0.844–0.937), 0.885 (95% CI, 0.802–0.968), and 0.863 (95% CI, 0.735–0.991) in the training, internal validation, and external validation cohorts, respectively (Fig. 2a–c). Across these cohorts, the sensitivities were 0.882, 0.765, and 0.889, and the negative predictive values (NPVs) were 0.974, 0.925, and 0.968, respectively. In the external validation cohort, the specificity and positive predictive value (PPV) of the fusion model were moderate, at 0.577 and 0.267, respectively. Nevertheless, its consistently high NPV supports the robust cross-cohort discrimination and generalization ability of the model **(**Table 1**)**. Confusion matrices of the six predictive models in the external validation cohort are shown in Fig. 3.

Table 1
Predictive performance of the six models across the three cohorts

Model	Cohort	AUC	95% CI	Accuracy	Sensitivity	Specificity	PPV	NPV	F1 score	Kappa	Youden index
Clinical	train	0.736	0.656–0.816	0.692	0.725	0.687	0.282	0.936	0.407	0.250	0.412
Clinical	Internal Validation	0.765	0.639–0.891	0.709	0.647	0.725	0.367	0.893	0.468	0.289	0.372
Clinical	External Validation	0.846	0.722–0.970	0.754	0.667	0.769	0.333	0.930	0.444	0.308	0.436
Tumor	train	0.760	0.693–0.827	0.632	0.784	0.607	0.253	0.943	0.383	0.209	0.391
Tumor	Internal Validation	0.687	0.544–0.830	0.686	0.706	0.681	0.353	0.904	0.471	0.281	0.387
Tumor	External Validation	0.768	0.612–0.924	0.672	0.667	0.673	0.261	0.921	0.375	0.207	0.340
P3	train	0.765	0.698–0.833	0.721	0.686	0.727	0.299	0.932	0.417	0.269	0.413
P3	Internal Validation	0.682	0.530–0.833	0.686	0.706	0.681	0.353	0.904	0.471	0.281	0.387
P3	External Validation	0.657	0.423–0.891	0.590	0.778	0.558	0.233	0.935	0.359	0.171	0.335
P5	train	0.799	0.735–0.863	0.709	0.784	0.697	0.305	0.950	0.440	0.291	0.481
P5	Internal Validation	0.786	0.680–0.892	0.686	0.882	0.638	0.375	0.957	0.526	0.344	0.520
P5	External Validation	0.590	0.441–0.738	0.475	0.889	0.404	0.205	0.955	0.333	0.123	0.293
Habitat	train	0.831	0.776–0.885	0.789	0.745	0.797	0.384	0.948	0.507	0.390	0.542
Habitat	Internal Validation	0.813	0.717–0.909	0.733	0.647	0.754	0.393	0.897	0.489	0.322	0.401
Habitat	External Validation	0.788	0.597–0.980	0.705	0.889	0.673	0.320	0.972	0.471	0.324	0.562
Fusion	train	0.891	0.844–0.937	0.778	0.882	0.760	0.385	0.974	0.536	0.418	0.642
Fusion	Internal Validation	0.885	0.802–0.968	0.721	0.765	0.710	0.394	0.925	0.520	0.351	0.475
Fusion	External Validation	0.863	0.735–0.991	0.623	0.889	0.577	0.267	0.968	0.410	0.237	0.466

Note. p53abn was treated as the positive class. Thresholds were selected in the training cohort using the Youden index and fixed for validation. Classification metrics were calculated at the locked thresholds. AUC 95% CIs were calculated using the DeLong method. p53abn, p53-abnormal; P3, 3-mm peritumoral region; P5, 5-mm peritumoral region; AUC, area under the receiver operating characteristic curve; CI, confidence interval; PPV, positive predictive value; NPV, negative predictive value.

DeLong tests showed that the fusion model significantly outperformed the clinical model in the training and internal validation cohorts, with AUC increases of 0.155 and 0.120, respectively (both $P < 0.05$). In the external validation cohort, the AUC of the fusion model was numerically higher than that of the clinical model, although the difference did not reach statistical significance. In addition, the fusion model significantly outperformed the P5 model across all three cohorts and significantly outperformed the Habitat model in the training and internal validation cohorts. In the external validation cohort, the AUC advantage of the fusion model over the Habitat model did not reach statistical significance (Fig. 4; **Additional file : Supplementary Table S4)**.

Notably, although habitat analysis, represented by the Habitat Rad-score, contributed the dominant discriminatory information, the fusion model still achieved additional reclassification improvement over the Habitat model alone in the external validation cohort (NRI = 0.543; IDI = 0.075). This finding indicates that, by systematically integrating baseline clinical features reflecting the systemic host status with peritumoral information reflecting tumor-margin invasion, the fusion model can effectively complement the limitations of intratumoral radiomics alone in cross-center generalization. It thereby enables more refined and robust risk reclassification and provides a solid methodological foundation for the subsequent construction of a visual nomogram aligned with real-world multidisciplinary clinical decision-making **(Additional file : Supplementary Table S5)**.

Regarding calibration and decision performance, the fusion model showed acceptable calibration across the three cohorts. The P values of the Hosmer–Lemeshow test were 0.778, 0.366, and 0.204, and the corresponding Brier scores were 0.078, 0.095, and 0.110, respectively **(**Fig. 2d–f**)**. DCA showed that the fusion model achieved the highest net benefit across a threshold probability range of 0.01–0.80 in the training cohort. In the internal validation cohort, its net benefit advantage was mainly observed within the threshold ranges of 0.01–0.10 and 0.15–0.80. In the external validation cohort, the fusion model maintained a positive net benefit within the range of 0.01–0.39, clearly outperforming the indiscriminate treat-all strategy, which assumes all patients to be at high risk for p53abn, and the treat-none strategy, which assumes all patients to be at low risk. However, its advantage over the other individual models was mainly limited to localized threshold intervals, including 0.01–0.07, 0.14–0.17, 0.23, and 0.25–0.26 **(**Fig. 2g–i**)**. These findings suggest that the fusion model has favorable calibration performance and potential clinical utility **(Additional file : Supplementary Table S6)**.

Model interpretation

To maximize clinical interpretability and facilitate individualized decision-making, we constructed a nomogram incorporating the fusion model and clinical variables, complemented by SHAP analysis to quantify feature contributions. The SHAP summary beeswarm plot showed that higher P5 Rad-scores and Habitat Rad-scores were the major drivers pushing predictions toward the p53abn subtype, thereby establishing the dominant contribution of imaging features over clinical variables. The partial dependence plots further confirmed that the model output increased monotonically with increasing values of these two imaging scores. Finally, representative waterfall plots deconstructed the predicted risk probabilities at the individual level and intuitively illustrated the collaborative predictive process of clinical and imaging features **(**Figs. 5 and 6**)**.

Discussion

Molecular classification has become a cornerstone of clinical risk stratification and treatment decision-making in endometrial cancer. Both the 2023 FIGO staging system and the latest ESGO–ESTRO–ESP guidelines strongly recommend integrating POLE, MMR, and p53 status assessment whenever feasible [19, 37]. Although the simplified ProMisE classification has substantially promoted the clinical translation of molecular classification through p53 IHC, IHC is intrinsically an indirect surrogate assay for TP53 gene status. In real-world practice, its interpretation may be affected by laboratory procedures, antibody clones, and atypical abnormal staining patterns, such as subclonal and cytoplasmic expression [15, 38–40]. In the present dual-center real-world diagnostic dataset, the overall discordance rate between conventional p53 IHC and gene sequencing, used as the reference standard, reached 10%, Cohen's κ was 0.64 **(Additional file : Supplementary Figure S2)**. This discordance illustrates the potential classification blind spots and risk of misclassification associated with reliance on conventional IHC alone, and it supports the use of molecular sequencing as the reference standard in this study. However, sequencing technology itself is limited by high economic cost and a relatively long reporting turnaround time. Moreover, conventional invasive local biopsy is highly susceptible to sampling error because of pronounced spatial heterogeneity, resulting in discordance between preoperative assessment and final postoperative pathology in nearly 20% of cases [17–18]. Against this background, a noninvasive predictive model based on preoperative MRI has clear complementary value. It can noninvasively extract spatial phenotypic information from the whole tumor and its marginal microenvironment at a panoramic scale, thereby providing timely molecular risk alerts for perioperative management.

In the field of radiomics-based prediction of molecular subtypes in endometrial cancer, previous studies have provided a series of valuable explorations. For example, Zhou et al. extracted multiparametric MRI features from the whole-tumor core region and the 3-mm peritumoral region, preliminarily demonstrating the feasibility of marginal microenvironmental information for predicting p53abn [41]. Yue et al. further attempted to combine handcrafted radiomic features, deep-learning features, and clinical information to construct an integrated predictive model [42]. In addition, Jin et al. developed an imaging model based on functional habitat

partitioning of tumors using diffusion-weighted imaging (DWI) and contrast-enhanced images, highlighting the importance of characterizing intratumoral spatial phenotypic heterogeneity [43].

Compared with these studies, which mainly focused on empirical validation of the feasibility of prediction using specific MRI sequences or a single spatial domain, the scientific contribution and methodological increment of the present study lie in the systematic head-to-head comparison and multidimensional integration of four spatial domains within a unified dual-center validation framework: the whole tumor (Tumor), peritumoral regions at different spatial scales (3 mm vs 5 mm), and intratumoral multiphysiological habitats. This design shifts the research focus from the peripheral question of “whether MRI can predict p53abn” to the clinically translational question of “which spatial imaging information provides the greatest incremental value and how stable cross-cohort prediction can be achieved.” Our findings strongly demonstrate that p53abn-related imaging signals are embedded simultaneously within intratumoral spatial heterogeneity and peritumoral microenvironmental remodeling.

In the present study, although the fusion model achieved the highest AUC across all cohorts, its absolute advantage over the individual models in the external validation cohort was mainly confined to localized risk-threshold windows. This phenomenon may reflect both biological and methodological mechanisms. Specifically, the Habitat Rad-score itself had already captured the dominant imaging phenotype associated with p53abn tumors, thereby attenuating the marginal gain that could be provided by additional clinical and peritumoral features. This interpretation was also supported by the global SHAP analysis.

Notably, the AUC of the P5 model was relatively low in the external validation cohort, suggesting that 5-mm peritumoral radiomic features may have certain limitations in cross-center generalization. This result does not negate the biological significance of the peritumoral region, but more likely reflects the higher sensitivity of peritumoral imaging features to intercenter heterogeneity. Compared with intratumoral regions, the P5 region is a spatial ring derived from outward expansion of the tumor boundary. Therefore, its feature stability may be more easily affected by tumor-boundary delineation errors, differences in myometrial thickness, intrauterine fluid, interference from necrosis or blood clots, inclusion of adjacent normal tissues, and differences in anatomical constraint masks. In addition, variations in DCE-MRI acquisition parameters, enhancement phase, slice thickness, spatial resolution, and image preprocessing workflows at the external center may also lead to distributional shifts in peritumoral features. Therefore, the reduced external validation performance of the P5 model more reasonably indicates a certain cross-center vulnerability of peritumoral microenvironmental signals, rather than a lack of predictive value of peritumoral information itself. These findings further suggest that the malignant biological signals associated with p53abn are more deeply embedded in the spatial heterogeneity of intratumoral functional subregions, whereas peritumoral and clinical features mainly provide complementary information to fill residual predictive gaps rather than serving as dominant predictors. Accordingly, this multidimensional fusion model should be positioned as an auxiliary screening tool for preoperative risk stratification, rather than a replacement for molecular pathological testing. Given its high negative predictive value in external validation (NPV = 0.968; Table 1), the model may be used in clinical practice to efficiently and noninvasively screen patients with an extremely low probability of mutation, thereby optimizing the allocation of medical resources. Alternatively, it may help identify high-risk individuals who should be prioritized for molecular testing review and intensified individualized pathological assessment.

It must be acknowledged that the present study, as well as related translational investigations, remains constrained by the inherent limitations of radiomics and habitat analysis. As high-throughput quantitative feature extraction approaches, radiomics and habitat analysis largely rely on high-dimensional abstract mathematical representations. Their major bottleneck is that high-order mathematical features cannot be directly and intuitively mapped to clear clinical or physical meanings, or to specific physiological or molecular biological pathways, in the same way as conventional clinical indicators or macroscopic anatomic pathology. Therefore, the underlying biological interpretability remains, to some extent, a black box. The model construction in this study is also subject to this common limitation. Although SHAP analysis was introduced to quantify feature weights, the microscopic pathophysiological mechanisms underlying specific habitat and peritumoral radiomic features remain to be further elucidated in future studies through histology-based multi-omics benchmarking, such as spatial transcriptomics or single-cell sequencing.

In addition, owing to the objective constraints of the retrospective dual-center design, the overall sample size of this study and the number of mutation-positive cases in the external validation cohort were relatively limited. This may, to some extent, have reduced the statistical power of several pairwise model comparisons. Future studies based on larger, multicenter, prospective, and workflow-standardized cohorts are still needed to further confirm the clinical utility and cross-institutional generalizability of the proposed predictive model.

Conclusions

A dual-center DCE-MRI fusion model integrating clinical predictors, 5-mm peritumoral radiomics, and intratumoral habitat radiomics showed good discrimination and external generalizability for p53abn endometrial cancer. The model may serve as a noninvasive adjunct for preoperative molecular risk stratification and prioritization for molecular testing, but it should not replace molecular pathological assessment.

Abbreviations

ADC
apparent diffusion coefficient
AdaBoost
adaptive boosting
AUC
area under the receiver operating characteristic curve
BMI
body mass index
CH
Calinski–Harabasz
CI
confidence interval
DCA
decision curve analysis
DCE-MRI
dynamic contrast-enhanced magnetic resonance imaging
DICOM
Digital Imaging and Communications in Medicine
EC
endometrial cancer
FIGO
International Federation of Gynecology and Obstetrics
Hb
hemoglobin
IBSI
Imaging Biomarker Standardization Initiative
ICC
intraclass correlation coefficient
IDI
integrated discrimination improvement
IHC
immunohistochemistry
IQR
interquartile range
LASSO
least absolute shrinkage and selection operator
LR
logistic regression
MLP
multilayer perceptron
MMR
mismatch repair

MRI
magnetic resonance imaging
MSI
microsatellite instability
NPV
negative predictive value
NRI
net reclassification improvement
NSE
neuron-specific enolase
OR
odds ratio
P3
3-mm peritumoral region
P5
5-mm peritumoral region
PACS
picture archiving and communication system
p53abn
p53-abnormal
PPV
positive predictive value
SHAP
SHapley Additive exPlanations
SVM
support vector machine
TCGA
The Cancer Genome Atlas
VOI
volume of interest.

Declarations

Ethics approval and consent to participate

This study was conducted in accordance with the Declaration of Helsinki and was approved by the Scientific Research Ethics Committee of Qilu Hospital of Shandong University (approval number: KYLL-202210-05501). The requirement for written informed consent was waived by the approving ethics committee because of the retrospective nature of the study.

Consent for publication

Not applicable.

Availability of data and materials

The datasets used and/or analyzed during the current study are not publicly available because they contain sensitive patient information but are available from the corresponding author on reasonable request.

Competing interests

The authors declare that they have no competing interests.

Funding

This work was supported by the National Key R&D Program of China (Grant No. 2022YFC2704304) and the National Natural Science Foundation of China (Grant No. 8237161678).

Authors' contributions

H.J. Dai and W.X. Guo carried out radiomics and bioinformatics analysis, established the experimental models, finished the original manuscript writing and figure production. Y. Liu undertook manuscript revision, data analysis and data verification. B.X. Yan and B.L. Lyu performed the delineation of imaging ROIs. F. Wang was in charge of MRI quality control, ROI examination and original manuscript review. J. Jiang proposed the research concept, conducted manuscript review, and provided comprehensive supervision and guidance throughout the whole study.

Acknowledgements

Not applicable.

Additional file 1

File format: .docx.

Title: Supplementary figures and tables.

Description: Supplementary Figure S1 presents voxel-wise local radiomic feature maps used for habitat analysis; Supplementary Figure S2 shows concordance between p53 immunohistochemistry and sequencing-based TP53 status; Supplementary Tables S1–S7 report baseline characteristics, clinical predictor regression results, candidate algorithm performance, pairwise DeLong comparisons, reclassification metrics, calibration statistics, and clustering quality metrics.

References

1. Siegel RL, Miller KD, Wagle NS, Jemal A. Cancer statistics, 2023. CA Cancer J Clin. 2023;73(1):17–48.
2. Contreras N-A, Sabadell J, Verdaguer P, Julià C, Fernández-Montolí M-E. Fertility-Sparing Approaches in Atypical Endometrial Hyperplasia and Endometrial Cancer Patients: Current Evidence and Future Directions. Int J Mol Sci. 2022;23(5):2531.
3. Shin DW, Jung KW, Ha J, Bae J. Conditional relative survival of patients with endometrial cancer: a Korean National Cancer Registry study. J Gynecol Oncol. 2022;33(2):e23.
4. Tronconi F, Nero C, Giudice E, Salutari V, Musacchio L, Ricci C, et al. Advanced and recurrent endometrial cancer: State of the art and future perspectives. Crit Rev Oncol Hematol. 2022;180:103851.
5. Cancer Genome Atlas Research N, Kandoth C, Schultz N, Cherniack AD, Akbani R, Liu Y, et al. Integrated genomic characterization of endometrial carcinoma. Nature. 2013;497(7447):67–73.
6. Yasuda M. New clinicopathological concept of endometrial carcinoma with integration of histological features and molecular profiles. Pathol Int. 2024;74(10):557–73.
7. Menendez-Santos M, Gonzalez-Baerga C, Taher D, Waters R, Virarkar M, Bhosale P. Endometrial Cancer: 2023 Revised FIGO Staging System and the Role of Imaging. Cancers (Basel). 2024;16(10):1869.
8. Ribeiro-Santos P, Martins Vieira C, Viana Veloso GG, Vieira Giannecchini G, Parenza Arenhardt M, Muller Gomes L, et al. Tailoring Endometrial Cancer Treatment Based on Molecular Pathology: Current Status and Possible Impacts on Systemic and Local Treatment. Int J Mol Sci. 2024;25(14):7742.
9. Dong YY, Zhao LY, Kang N, Wang YQ, Li H, Wang ZQ, et al. Chinese expert consensus on the clinical application of molecular classification in endometrial cancer (2024 edition). Chin J Practical Gynecol Obstet. 2024;40(6):638–44.
10. Chang Z, Talukdar S, Mullany SA, Winterhoff B. Molecular characterization of endometrial cancer and therapeutic implications. Curr Opin Obstet Gynecol. 2019;31(1):24–30.
11. Rodolakis A, Scambia G, Planchamp F, Acien M, Di Spiezio Sardo A, Farrugia M, et al. ESGO/ESHRE/ESGE Guidelines for the fertility-sparing treatment of patients with endometrial carcinoma. Hum Reprod Open. 2023;2023(1):hoac057.
12. Peng H, Jiang J, Li L, Hao Z, Lian H, Du H, et al. Mismatch repair deficiency and abnormal p53 expression has significant predictive value for progesterone resistance and endometrial tumorigenesis in patients with endometrial atypical hyperplasia

receiving fertility-preserving treatment. Gynecol Oncol. 2024;186:154–60.
13. Talhouk A, McConechy MK, Leung S, Li-Chang HH, Kwon JS, Melnyk N, et al. A clinically applicable molecular-based classification for endometrial cancers. Br J Cancer. 2015;113(2):299–310.
14. Eich ML, Siemanowsk-Hrach J, Drebber U, Friedrichs N, Mallmann P, Domrose C, et al. Assessment of p53 in Endometrial Carcinoma Biopsy and Corresponding Hysterectomy Cases in a Real-World Setting: Which Cases Need Molecular Work-Up? Cancers (Basel). 2025;17(9):1506.
15. Vermij L, Leon-Castillo A, Singh N, Powell ME, Edmondson RJ, Genestie C, et al. p53 immunohistochemistry in endometrial cancer: clinical and molecular correlates in the PORTEC-3 trial. Mod Pathol. 2022;35(10):1475–83.
16. Murali R, Soslow RA, Weigelt B. Classification of endometrial carcinoma: more than two types. Lancet Oncol. 2014;15(7):e268–78.
17. Otero-García MM, Mesa-Álvarez A, Nikolic O, Blanco-Lobato P, Basta-Nikolic M, de Llano-Ortega RM, et al. Role of MRI in staging and follow-up of endometrial and cervical cancer: pitfalls and mimickers. Insights Imaging. 2019;10(1):19.
18. Han G, Sidhu D, Duggan MA, Arseneau J, Cesari M, Clement PB, et al. Reproducibility of histological cell type in high-grade endometrial carcinoma. Mod Pathol. 2013;26(12):1594–604.
19. Concin N, Matias-Guiu X, Cibula D, et al. ESGO-ESTRO-ESP guidelines for the management of patients with endometrial carcinoma: update 2025. Lancet Oncol. 2025;26(8):e423–35.
20. Wilson EM, Huang R, Jones KD, Hagemann IS, Temkin SM, McAlpine JN, et al. Challenges in implementation of molecular classification in early stage endometrial cancer-An NRG Oncology cooperative group mixed-methods study. Cancer. 2025;131(1):e35596.
21. Koh W-J, Abu-Rustum NR, Bean S, Bradley K, Campos SM, Cho KR, et al. Uterine Neoplasms, Version 1.2018, NCCN Clinical Practice Guidelines in Oncology. J Natl Compr Canc Netw. 2018;16(2):170–99.
22. Zahra MA, Martin CW. Commentary on: Staging of endometrial carcinomas with MRI using traditional and novel MRI techniques. Clin Radiol. 2012;67(1):13–4.
23. Yu YY, Zhang R, Dong RT, Hu QY, Yu T, Liu F, et al. Feasibility of an ADC-based radiomics model for predicting pelvic lymph node metastases in patients with stage IB–IIA cervical squamous cell carcinoma. Br J Radiol. 2019;92(1097):20180986.
24. Wang XY, Wei MX, Chen SQ. Preoperative prediction of FIGO stage in epithelial ovarian cancer based on peritumoral and intratumoral radiomics models from T2-weighted MRI. Chin J Magn Reson Imaging. 2024;15(6):100–6.
25. Wu P-Q, Guo F-L, Wang J, Gao Y, Feng S-T, Chen S-L, et al. Development and validation of a dynamic contrast-enhanced magnetic resonance imaging-based habitat and peritumoral radiomic model to predict axillary lymph node metastasis in patients with breast cancer: a retrospective study. Quant Imaging Med Surg. 2024;14(12):8211–26.
26. Lambin P, Rios-Velazquez E, Leijenaar R, Carvalho S, van Stiphout RGPM, Granton P, et al. Radiomics: Extracting more information from medical images using advanced feature analysis. Eur J Cancer. 2012;48(4):441–6.
27. Gillies RJ, Kinahan PE, Hricak H. Radiomics: images are more than pictures, they are data. Radiology. 2016;278(2):563–77.
28. Jiang W, Wang H, Cui Y. Radiomics-Based Machine Learning for the Detection of Myometrial Invasion in Endometrial Cancer: Systematic Review and Meta-Analysis. J Med Internet Res. 2025;27:e78809.
29. Lefebvre TL, Ueno Y, Dohan A, Chatterjee A, Vallieres M, Winter-Reinhold E, et al. Development and Validation of Multiparametric MRI-based Radiomics Models for Preoperative Risk Stratification of Endometrial Cancer. Radiology. 2022;305(2):375–86.
30. Donato VD, Kontopantelis E, Cuccu I, Sgamba L, D'Augè TG, Pernazza A, et al. Magnetic resonance imaging-radiomics in endometrial cancer: A systematic review and meta-analysis. Int J Gynecol Cancer. 2023;33(7):1070–6.
31. Sun Y, Zhang J, Wang Y, Zhang X, Chen Y. The value of multi-sequence magnetic resonance imaging and whole-tumor apparent diffusion coefficient histogram analysis in differentiating p53 abnormal from non-p53 abnormal endometrial carcinoma. Front Oncol. 2025;15:1565152.
32. Gatenby RA, Grove O, Gillies RJ. Quantitative imaging in cancer evolution and ecology. Radiology. 2013;269(1):8–15.
33. Napel S, Mu W, Jardim-Perassi BV, Aerts H, Gillies RJ. Quantitative imaging of cancer in the postgenomic era: Radio(geno)mics, deep learning, and habitats. Cancer. 2018;124(24):4633–49.
34. Kim M, Park JE, Kim HS, Kim N, Park SY, Kim YH, et al. Spatiotemporal habitats from multiparametric physiologic MRI distinguish tumor progression from treatment-related change in post-treatment glioblastoma. Eur Radiol. 2021;31(8):6374–83.

35. Sagreiya H. Finding the Pieces to Treat the Whole: Using Radiomics to Identify Tumor Habitats. Radiol Artif Intell. 2024;6(2):e230547.
36. Ren J, Cui T, Li X, Zhang Y, Shen Z, Yue Y. Integrative intratumoral and peritumoral radiomic model for predicting endometrial cancer grade. Oncol Lett. 2025;30(4):482.
37. Berek JS, Matias-Guiu X, Creutzberg C, Fotopoulou C, Gaffney D, Kehoe S, et al. FIGO staging of endometrial cancer: 2023. Int J Gynaecol Obstet. 2023;162(2):383–94.
38. Singh N, Piskorz AM, Bosse T, Jimenez-Linan M, Rous B, Brenton JD, et al. p53 immunohistochemistry is an accurate surrogate for TP53 mutational analysis in endometrial carcinoma biopsies. J Pathol. 2020;250(3):336–45.
39. Thiel KW, Devor EJ, Filiaci VL, Mutch D, Moxley K, Alvarez Secord A, et al. TP53 Sequencing and p53 Immunohistochemistry Predict Outcomes When Bevacizumab Is Added to Frontline Chemotherapy in Endometrial Cancer: An NRG Oncology/Gynecologic Oncology Group Study. J Clin Oncol. 2022;40(28):3289–300.
40. Raffone A, Travaglino A, Cerbone M, De Luca C, Russo D, Di Maio A, et al. Diagnostic accuracy of p53 immunohistochemistry as surrogate of TP53 sequencing in endometrial cancer. Pathol Res Pract. 2020;216(8):153025.
41. Zhou J, Yu X, Cui Y, Zhou Q, Xu Q, Zhang X, et al. Prediction of molecular subtypes of endometrial cancer patients on the basis of intratumoral and peritumoral radiomic features from multiparametric MR images. Eur J Radiol. 2025;187:112110.
42. Yue W, Han R, Wang H, Liang X, Zhang H, Li H, et al. Development and validation of clinical-radiomics deep learning model based on MRI for endometrial cancer molecular subtypes classification. Insights Imaging. 2025;16:107.
43. Jin W, Zhang H, Ning Y, Chen X, Zhang G, Li H, et al. Development and Validation of an Explainable MRI-Based Habitat Radiomics Model for Predicting p53-Abnormal Endometrial Cancer: A Multicentre Feasibility Study. J Imaging Inf Med. 2026;39(2):1547–57.

Figures

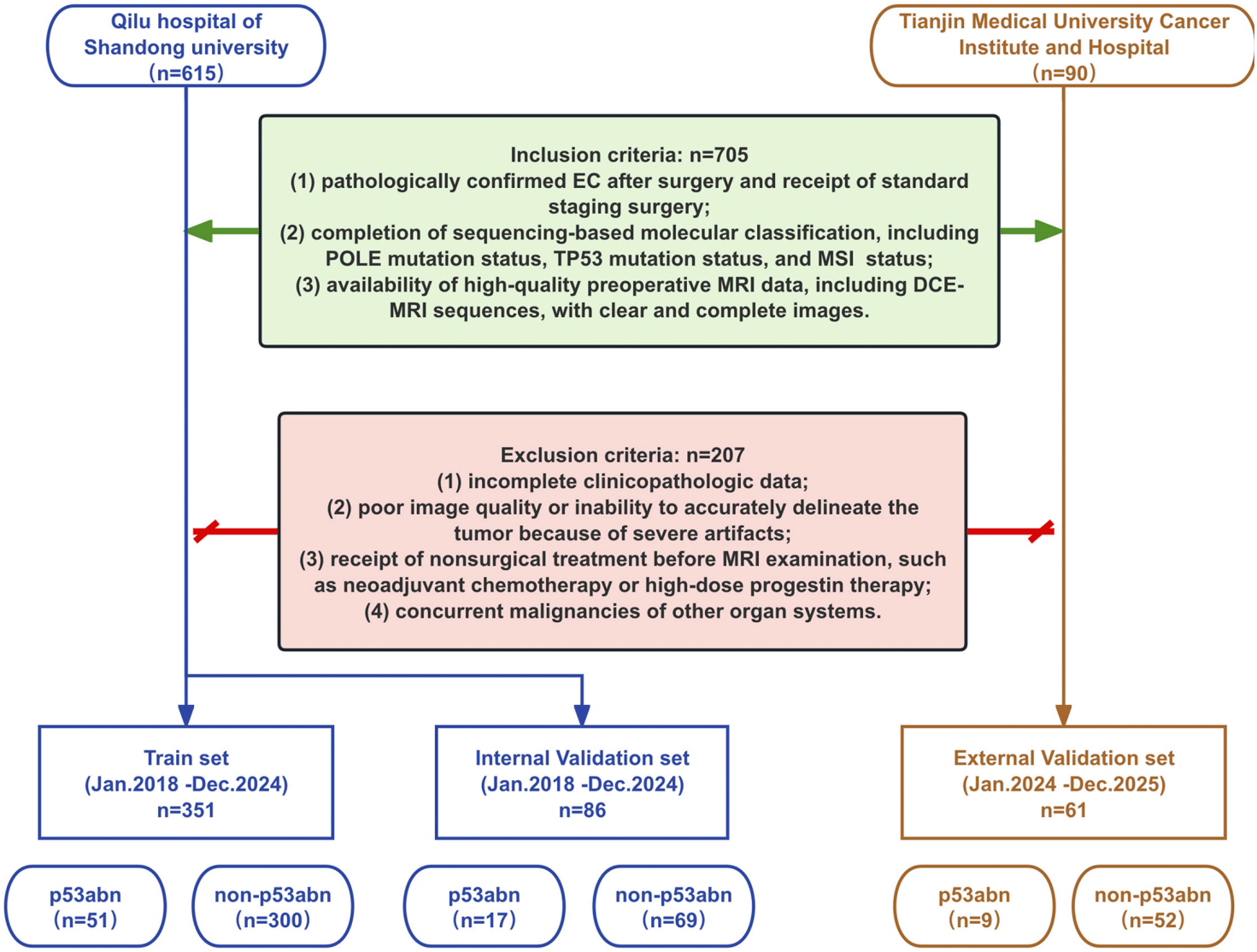


Figure 1

Flowchart of dual-center patient recruitment and cohort allocation.

A total of 705 patients with endometrial cancer (EC) from two institutions (Qilu Hospital of Shandong University and Tianjin Medical University Cancer Institute and Hospital) were initially evaluated. Following the application of rigorous inclusion and exclusion criteria, 498 eligible patients were enrolled. The dual-track visual layout illustrates the independent processing and logical separation of the internal cohort (blue track, divided into a training set and an internal validation set) and the external validation cohort (brown track).

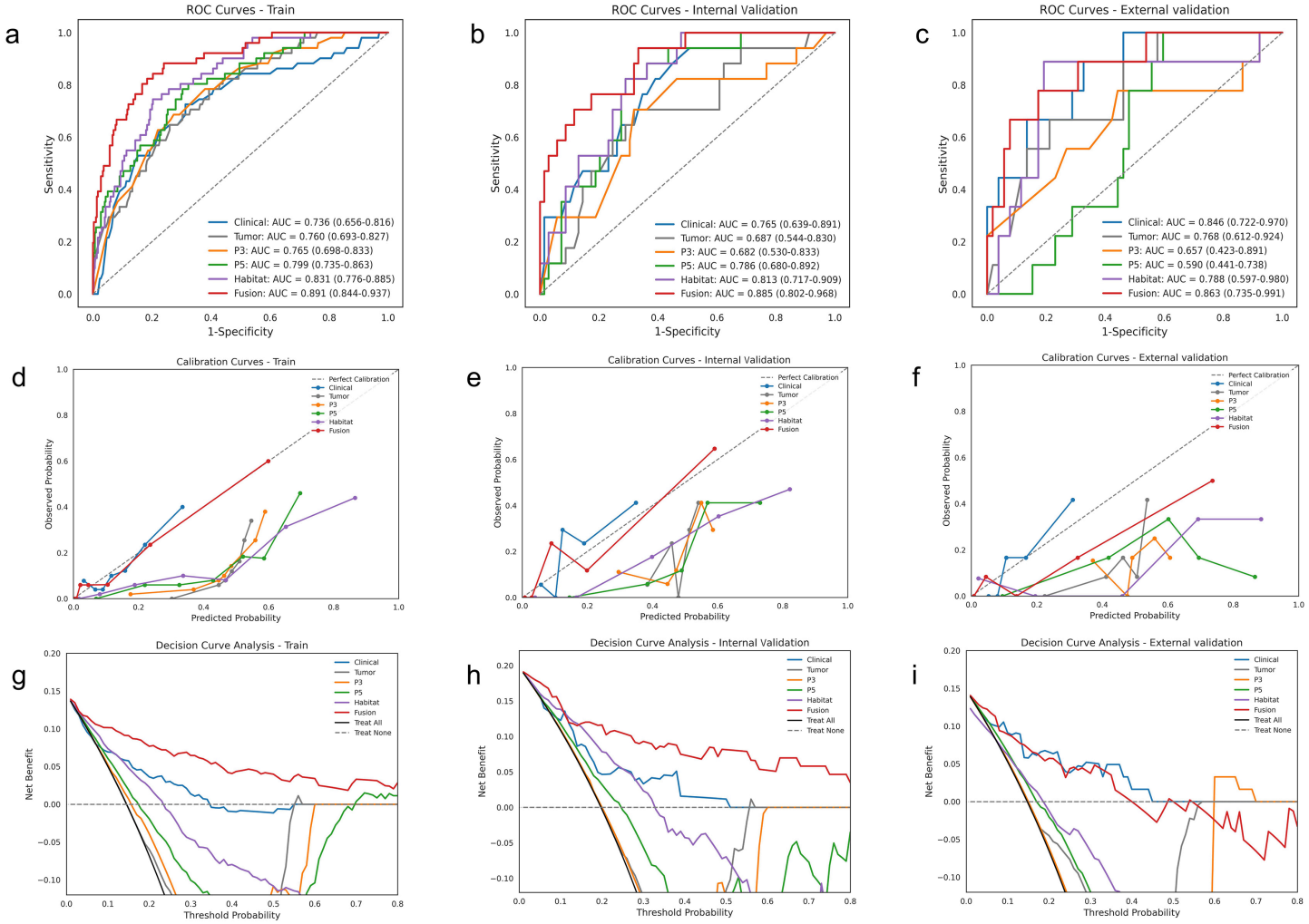


Figure 2

Predictive performance and clinical utility across the training and validation cohorts.

(a–c) Receiver operating characteristic (ROC) curves comparing the discriminative performance of the Clinical, Tumor, P3, P5, Habitat, and Fusion models in the training (a), internal validation (b), and external validation (c) cohorts. (d–f) Calibration curves of the predictive models in the training (d), internal validation (e), and external validation (f) cohorts. The diagonal dashed line represents perfect calibration, while the solid lines represent the observed performance of each model. (g–i) Decision curve analysis (DCA) for assessing the clinical net benefit of the models in the training (g), internal validation (h), and external validation (i) cohorts. The solid black line indicates the extreme baseline assumption that all patients are at high risk for the p53abn subtype (Treat-All), whereas the dashed grey line indicates the assumption that all patients are at low risk (Treat-None).

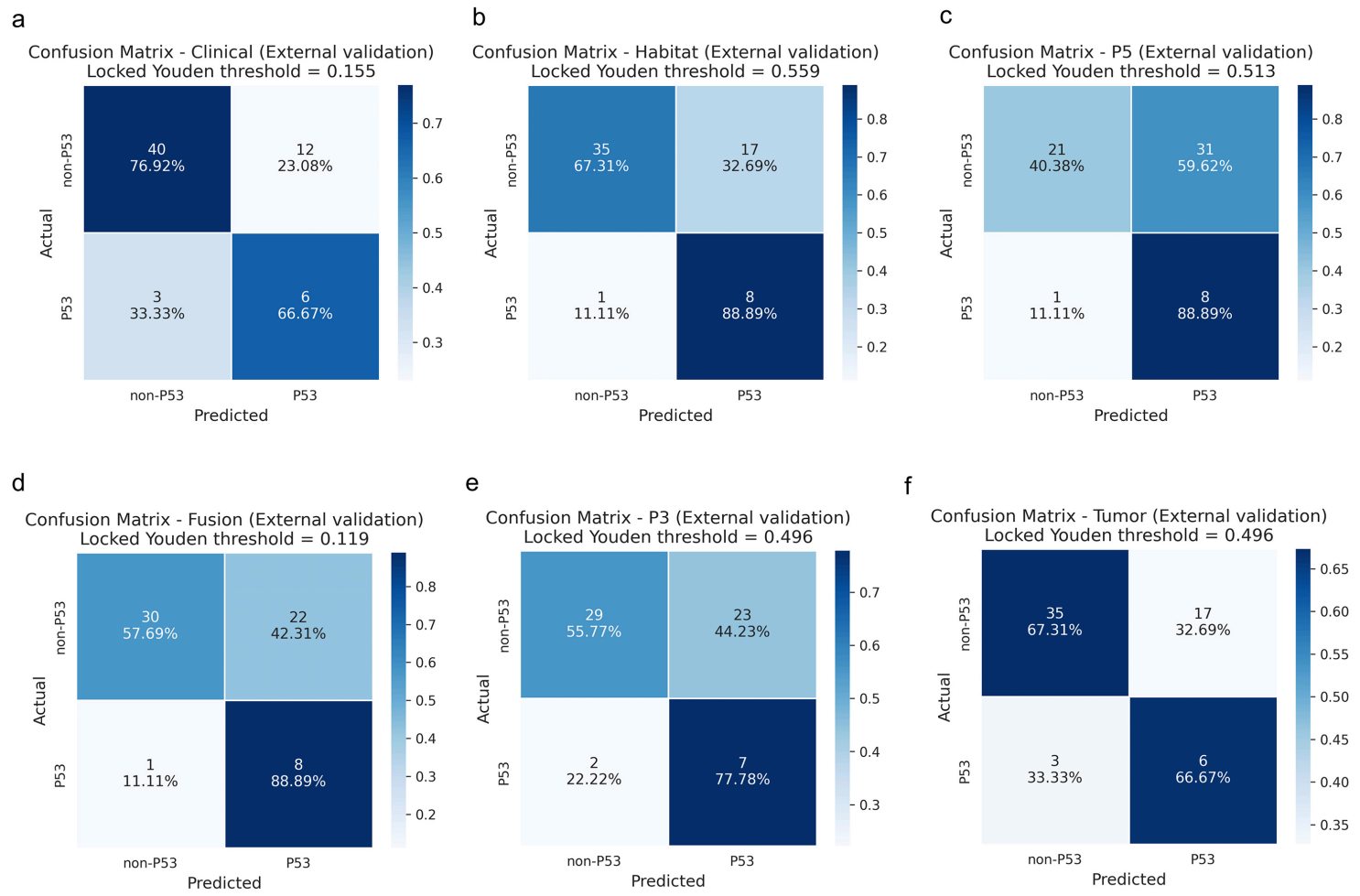


Figure 3

Confusion matrices of the six models in the external validation cohort.

(a–f) Confusion matrices for the Clinical (a), Habitat (b), P5 (c), Fusion (d), P3 (e), and Tumor (f) models. The matrices detail the actual versus predicted classifications for the p53abn and non-p53abn subtypes, with cell counts and row percentages shown for each model at the independently locked optimal Youden index thresholds.

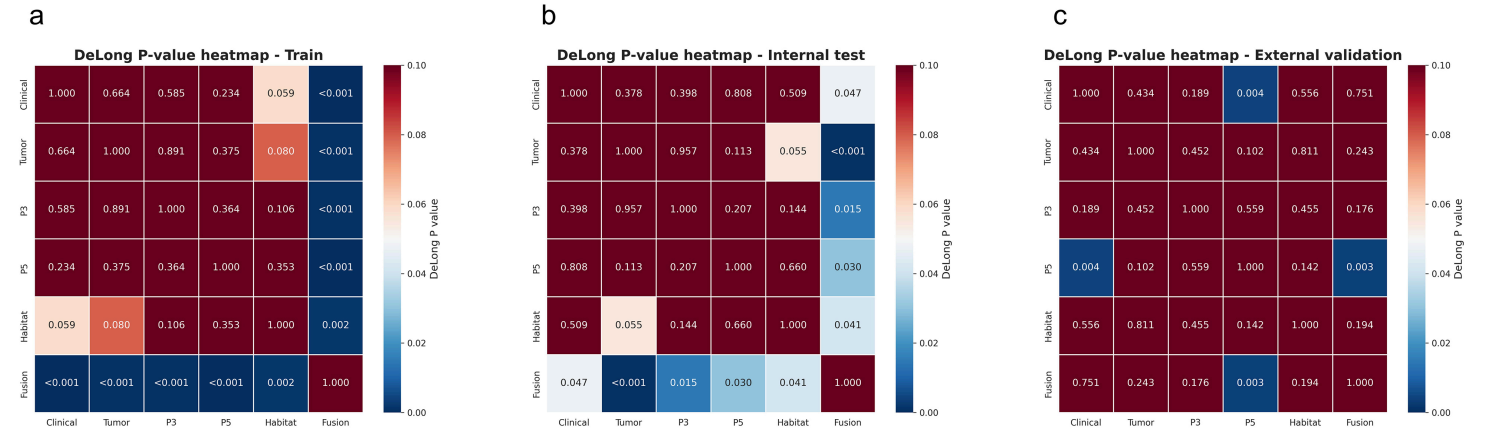


Figure 4

DeLong test heatmaps for pairwise model comparisons across the three cohorts.

(a–c) Heatmaps illustrating the statistical significance of differences in the area under the curve (AUC) among the Clinical, Tumor, P3, P5, Habitat, and Fusion models in the training (a), internal validation (b), and external validation (c) cohorts. The color gradients and annotated numerical values denote the exact P-values derived from the DeLong tests.

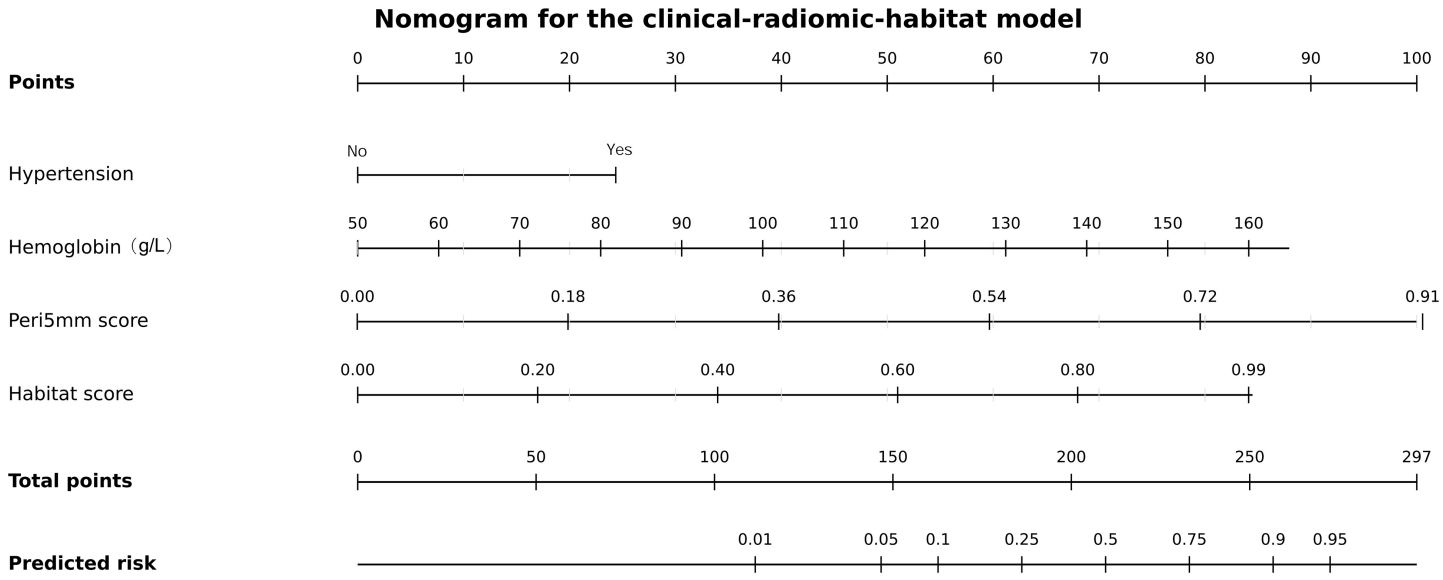


Figure 5

Nomogram based on the fusion model.

The nomogram developed based on the Fusion model, integrating the independent clinical predictors (Hypertension and Hemoglobin) with the optimal spatial radiomic signatures (Peri5mm score and Habitat score) for the individualized preoperative prediction of p53abn probability.

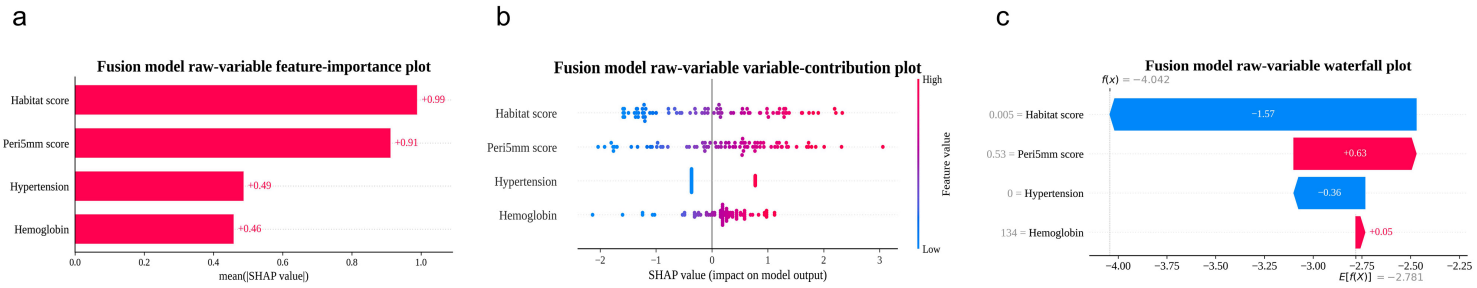


Figure 6

SHAP-based interpretability analysis of the multidimensional fusion model.

(a) Global feature importance plot based on mean absolute SHAP values, identifying the Habitat score and Peri5mm score as the most substantial contributors driving the fusion model's predictions. (b) SHAP summary plot illustrating the distribution, magnitude, and direction of each specific feature's impact on the model's output. Red indicates higher feature values, while blue indicates lower feature values. (c) A representative SHAP waterfall plot illustrating the individualized predictive reasoning for a specific patient. The model initiates from the population's baseline expected risk value (E[f(X)] = -2.781). The plot then visually dissects how this patient's specific inputs (shown in grey on the left) cumulatively shift the risk. Specifically, the patient's Hemoglobin level of 134 and Peri5mm score of 0.53 marginally increase the predicted risk (red arrows, +0.05 and +0.63, respectively). Conversely, the absence of Hypertension [0] and a critically low Habitat score of 0.005 substantially decrease the risk (blue arrows, -0.36 and -1.57, respectively). Summing these positive and negative quantitative contributions yields the final individualized prediction score (f(x) = -4.042), thereby providing a transparent, step-by-step rationale for ruling out the p53abn subtype in this case.

Supplementary Files

This is a list of supplementary files associated with this preprint. Click to download.

- SupplementaryFigure1.jpg
- SupplementaryFigure2.jpg
- SupplementaryTableS1.docx
- SupplementaryTableS2.docx
- SupplementaryTableS3.docx
- SupplementaryTableS4.docx
- SupplementaryTableS5.docx
- SupplementaryTableS6.docx
- SupplementaryTableS7.docx
- abstractgraphic.pdf